

Cite this: *Chem. Sci.*, 2024, 15, 5368

All publication charges for this article have been paid for by the Royal Society of Chemistry

# Sunlight-driven and gram-scale vanillin production via Mn-defected $\gamma$ -MnO<sub>2</sub> catalyst in aqueous environment†

Qingping Ke,<sup>a</sup> Yurong Zhang,<sup>a</sup> Chao Wan,<sup>a</sup> Jun Tang,<sup>a</sup> Shenglai Li,<sup>c</sup> Xu Guo,<sup>a</sup> Minsu Han,<sup>d</sup> Takashi Hamada,<sup>e</sup> Sameh M. Osman,<sup>f</sup> Yunqing Kang<sup>g</sup> and Yusuke Yamauchi<sup>deg</sup>

The production of vanillin from biomass offers a sustainable route for synthesizing daily-use chemicals. However, achieving sunlight-driven vanillin synthesis through H<sub>2</sub>O activation in an aqueous environment poses challenges due to the high barrier of H<sub>2</sub>O dissociation. In this study, we have successfully developed an efficient approach for gram-scale vanillin synthesis in an aqueous reaction, employing Mn-defected  $\gamma$ -MnO<sub>2</sub> as a photocatalyst at room temperature. Density functional theory calculations reveal that the presence of defective Mn species (Mn<sup>3+</sup>) significantly enhances the adsorption of vanillyl alcohol and H<sub>2</sub>O onto the surface of the  $\gamma$ -MnO<sub>2</sub> catalyst. Hydroxyl radical (<sup>•</sup>OH) species are formed through H<sub>2</sub>O activation with the assistance of sunlight, playing a pivotal role as oxygen-reactive species in the oxidation of vanillyl alcohol into vanillin. The Mn-defected  $\gamma$ -MnO<sub>2</sub> catalyst exhibits exceptional performance, achieving up to 93.4% conversion of vanillyl alcohol and 95.7% selectivity of vanillin under sunlight. Notably, even in a laboratory setting during the daytime, the Mn-defected  $\gamma$ -MnO<sub>2</sub> catalyst demonstrates significantly higher catalytic performance compared to the dark environment. This work presents a highly effective and promising strategy for low-cost and environmentally benign vanillin synthesis.

Received 24th October 2023  
Accepted 15th January 2024

DOI: 10.1039/d3sc05654f

rsc.li/chemical-science

## Introduction

Vanillin, a highly popular spice worldwide, is extensively used in food additives, perfumes, and daily-use chemicals.<sup>1</sup> Traditionally, it is derived from fossil fuels through the Solvay route,<sup>2</sup> which involves the oxidation of vanillyl alcohol to vanillin using methanol as a solvent. In addition to the Solvay route, about

15% of vanillin is directly isolated from depolymerized lignin derivatives through upcycling,<sup>3–5</sup> presenting an eco-friendly method that avoids reliance on fossil fuels. However, only approximately 2% of lignin currently undergoes conversion to value-added chemicals, with the remaining 98% being incinerated for energy in the pulp and paper industry. Consequently, a significant challenge in terms of sustainability and environmental protection lies in the valorization of lignin.<sup>6–9</sup> Among potential approaches, the synthetic vanillin market, producing around 17 000 tons per year, primarily relies on fossil-based routes. Chemical conversions of lignin-derived compounds, such as vanillyl alcohol, offer a sustainable and cost-effective route to replenish the synthetic vanillin market.<sup>10</sup> Unfortunately, most lignin-to-vanillin processes operate in organic solvents, requiring high temperature/O<sub>2</sub> pressure,<sup>6</sup> and consuming artificial energy due to recrystallization and solvent extraction steps.<sup>11</sup> In response to these drawbacks, the development of sunlight-driven organic transformations through the construction of novel heterogeneous catalyst materials that are efficient and separable even in aqueous reactions holds promise for the sustainable synthesis of valuable chemicals.<sup>12</sup>

The water-participated route for alcohol oxidation signifies a noteworthy advancement in organic synthesis,<sup>13</sup> offering a novel and sustainable approach to vanillin synthesis. However, this oxidation process encounters challenges due to the energy-

<sup>a</sup>School of Chemistry and Chemical Engineering, Anhui University of Technology, Ma'anshan 243002, China. E-mail: wanchao@zju.edu.cn

<sup>b</sup>College of Chemical and Biological Engineering, Zhejiang University, Hangzhou 310058, China

<sup>c</sup>Department of Materials Science and Chemical Engineering, Stony Brook University, New York 11794, USA

<sup>d</sup>Australian Institute for Bioengineering and Nanotechnology (AIBN), The University of Queensland, Brisbane, Queensland 4072, Australia. E-mail: minsu.han@uq.edu.au

<sup>e</sup>Department of Materials Process Engineering, Graduate School of Engineering, Nagoya University, Nagoya 464-8603, Japan

<sup>f</sup>Chemistry Department, College of Science, King Saud University, P.O. Box 2455, Riyadh, 11451, Saudi Arabia

<sup>g</sup>Research Center for Materials Nanoarchitectonics (MANA), National Institute for Materials Science (NIMS), 1-1 Namiki, Tsukuba, Ibaraki 305-0044, Japan. E-mail: yqkang@toki.waseda.jp

<sup>h</sup>Department of Chemical and Biomolecular Engineering, Yonsei University, Seoul 03722, South Korea

† Electronic supplementary information (ESI) available. See DOI: <https://doi.org/10.1039/d3sc05654f>

demanding O–H bond activation of H<sub>2</sub>O.<sup>14</sup> While light-driven H<sub>2</sub>O dissociation has emerged as an attractive method to activate the O–H bond, the limited success cases of this process mainly rely on noble metal catalysts and artificial light sources, such as a Xenon lamp.<sup>15</sup> An effective strategy for manipulating the H<sub>2</sub>O dissociation pathway, including the energy requirement for O–H bond activation and the chemical nature of the active metal/oxygen species, involves the coordination engineering of metal oxide catalysts. The coordination engineering of bismuth (Bi) and oxygen (O) sites in the BiOBr catalyst has successfully demonstrated the enhancement of ethylbenzene oxidation through sunlight-driven reduction of the adsorption barrier for H<sub>2</sub>O activation.<sup>15</sup> However, investigations into the sunlight-driven synthesis of vanillin in an aqueous environment using metal oxides remain relatively scarce.

MnO<sub>2</sub>, a transition metal oxide, has garnered significant attention as a heterogeneous catalyst for catalytic oxidation reactions, owing to its inherent advantages, including multivalence (Mn<sup>2+</sup>, Mn<sup>3+</sup>, and Mn<sup>4+</sup>)<sup>16</sup> and a variable structure ( $\alpha$ -,  $\gamma$ -,  $\epsilon$ -, R-, and  $\beta$ -MnO<sub>2</sub>).<sup>17</sup> Among these structures,  $\gamma$ -MnO<sub>2</sub>, characterized by a disordered structure comprising the intergrowth of  $\beta$ -MnO<sub>2</sub> and R-MnO<sub>2</sub>, stands out as one of the most extensively studied manganese dioxides.<sup>18,19</sup> Herein, we report the successful fabrication of a Mn-defected  $\gamma$ -MnO<sub>2</sub> catalyst for the water-participated oxidation of vanillyl alcohol to vanillin in an aqueous reaction under sunlight illumination. Our approach offers several notable advantages (Table S1†): (1) the use of H<sub>2</sub>O as a green reaction medium and oxygen source, promoting environmental sustainability; (2) utilization of sunlight as the energy source for H<sub>2</sub>O activation, reducing reliance on artificial light sources; (3) conducting the reaction at room temperature, minimizing energy requirements, and enabling milder reaction conditions; (4) the possibility of achieving gram-scale reactions, allowing for large-scale production; (5) a separable, additive-free, and carbon-efficient protocol, enhancing the overall efficiency and sustainability of the process.

## Results and discussion

$\gamma$ -MnO<sub>2</sub> catalysts with defects in Mn species were obtained through a hydrothermal process (Fig. 1a, see ESI† for preparation details). The crystal structures of the as-prepared  $\gamma$ -MnO<sub>2</sub> catalysts were characterized using powder X-ray diffraction (PXRD). As shown in Fig. 1b and S1,† regardless of the amount of urea, the synthesized  $\gamma$ -MnO<sub>2</sub>,  $\gamma$ -MnO<sub>2</sub>(1), and  $\gamma$ -MnO<sub>2</sub>(10) catalysts (1 and 10 referring to the feeding amount of urea) exhibit peaks at  $2\theta = 22.4^\circ$ ,  $37.0^\circ$ ,  $42.3^\circ$ , and  $56.0^\circ$ , corresponding to the (120), (131), (300), and (160) planes, respectively. These planes are well indexed to the layered  $\gamma$ -MnO<sub>2</sub> (JCPDS-14-0644).<sup>20,21</sup> For comparison, MnO<sub>2</sub> catalysts with different crystal structures, such as  $\alpha$ -MnO<sub>2</sub>,  $\beta$ -MnO<sub>2</sub>, and  $\epsilon$ -MnO<sub>2</sub>, were synthesized using different raw materials<sup>22</sup> and characterized by PXRD (Fig. S2†). Scanning electron microscopy (SEM) and transmission electron microscopy (TEM) analyses reveal that the as-prepared  $\gamma$ -MnO<sub>2</sub> particles exhibit a spherical shape with a size of 6  $\mu$ m (Fig. 1c), in which nanorods with a thickness of several tens of nanometers are assembled (Fig. 1d and e). In the selected area electron

diffraction (SAED) pattern (Fig. 1f) and high-resolution TEM (HRTEM) image (Fig. 1g) of  $\gamma$ -MnO<sub>2</sub> nanorods, crystalline spaces of 0.24 and 0.39 nm corresponding to the (131)<sup>23,24</sup> and (120)<sup>25,26</sup> planes of  $\gamma$ -MnO<sub>2</sub>, respectively, are observed, consistent with the XRD results. Energy-dispersive X-ray spectroscopy (EDS) mapping confirms the uniform dispersion of Mn and O throughout the  $\gamma$ -MnO<sub>2</sub> particle (Fig. 1h). Notably, no N residue is observed for  $\gamma$ -MnO<sub>2</sub> according to X-ray photoelectron spectroscopy (XPS) characterization (Fig. S3a†). Both  $\gamma$ -MnO<sub>2</sub>(1) and  $\gamma$ -MnO<sub>2</sub>(10) particles synthesized in the presence of urea exhibit a morphology observed in SEM images (Fig. S4†), a crystal structure observed in TEM images (Fig. S5†), and N<sub>2</sub> adsorption-desorption isotherms (Fig. S6†) similar to  $\gamma$ -MnO<sub>2</sub> synthesized without urea.

XPS is a regular and powerful tool used to identify the surface elemental species and electronic states of materials. Fig. 2 and S7–S10† show the Mn 3s, Mn 2p, and O 1s XPS patterns of the as-prepared  $\alpha$ -MnO<sub>2</sub>,  $\beta$ -MnO<sub>2</sub>,  $\epsilon$ -MnO<sub>2</sub>, and  $\gamma$ -MnO<sub>2</sub> catalysts. The  $\Delta E_s$  (binding energy between two peaks of Mn 3s multiplet splitting) of the  $\gamma$ -MnO<sub>2</sub> catalysts in the range of 4.5–5.1 eV confirm the presence of Mn<sup>3+</sup> species (Fig. 2a),<sup>27</sup> indicating the coexistence of both Mn<sup>3+</sup> and Mn<sup>4+</sup> species in these catalysts. The average oxidation states (AOS) of Mn species are calculated using the following formula.<sup>28,29</sup>

$$\text{AOS} = 8.956 - 1.126\Delta E_s$$

As shown in Fig. 2a, the calculated AOS values are 3.2, 3.4, and 3.9 for  $\gamma$ -MnO<sub>2</sub>,  $\gamma$ -MnO<sub>2</sub>(1), and  $\gamma$ -MnO<sub>2</sub>(10), respectively, consistent with the Mn<sup>3+</sup>/Mn<sup>4+</sup> ratios (Fig. S7a–c,† Mn<sup>3+</sup>/Mn<sup>4+</sup> = 1.54, 1.36, and 1.28 for  $\gamma$ -MnO<sub>2</sub>,  $\gamma$ -MnO<sub>2</sub>(1), and  $\gamma$ -MnO<sub>2</sub>(10) particles, respectively). It's worth noting that the oxygen defects (O<sub>d</sub>) remain almost constant in  $\gamma$ -MnO<sub>2</sub>,  $\gamma$ -MnO<sub>2</sub>(1), and  $\gamma$ -MnO<sub>2</sub>(10) (37.2–39.3%), as shown in Fig. S7d–f.† Interestingly, MnO<sub>2</sub> with different crystal structures exhibits varying degrees of Mn defects (Mn<sub>d</sub>) associated with Mn<sup>3+</sup> species (Fig. 2b). The calculated AOS values are 3.8, 3.8, and 4.0 for  $\alpha$ -MnO<sub>2</sub>,  $\beta$ -MnO<sub>2</sub>, and  $\epsilon$ -MnO<sub>2</sub>, respectively, with corresponding ratios of Mn<sup>3+</sup>/Mn<sup>4+</sup> being 1.51, 1.50, and 1.47 (Fig. S8†). The highest ratio of Mn<sup>3+</sup>/Mn<sup>4+</sup> (1.54) in  $\gamma$ -MnO<sub>2</sub> among the MnO<sub>2</sub> is ascribed to its most abundant Mn<sub>d</sub> caused by the coordination unsaturation between the lattice oxygen and lattice Mn. Typically, unsaturated metal species and O<sub>d</sub> species, which are active in various oxidation reactions, coexist in metal oxides.<sup>30,31</sup> It is well known that Mn<sub>d</sub>, caused by coordination unsaturation between lattice oxygen and lattice Mn, can be tuned by inducing O<sub>d</sub> or adjusting non-metal dopant amounts.<sup>32–34</sup> Contrary to the almost constant presence of O<sub>d</sub> species (Fig. 2c), significantly higher N dopants are observed in  $\gamma$ -MnO<sub>2</sub>(1) and  $\gamma$ -MnO<sub>2</sub>(10) compared to  $\gamma$ -MnO<sub>2</sub> (Fig. S3†).<sup>35</sup> The N anionic (N<sup>3–</sup>) dopants possess excess negative charges compared to the O anionic (O<sup>2–</sup>),<sup>36</sup> leading to a higher AOS of Mn species due to the charge compensation for higher N dopants. A similar higher AOS of Mn species in MnO<sub>2</sub> was previously observed with boron doping.<sup>37</sup> For comparison, we synthesized  $\alpha$ -MnO<sub>2</sub> catalysts with different O<sub>d</sub> sites. As shown in Fig. 2d and S9,† surface O<sub>d</sub> sites in  $\alpha$ -MnO<sub>2</sub> catalysts significantly increase after the addition of urea during



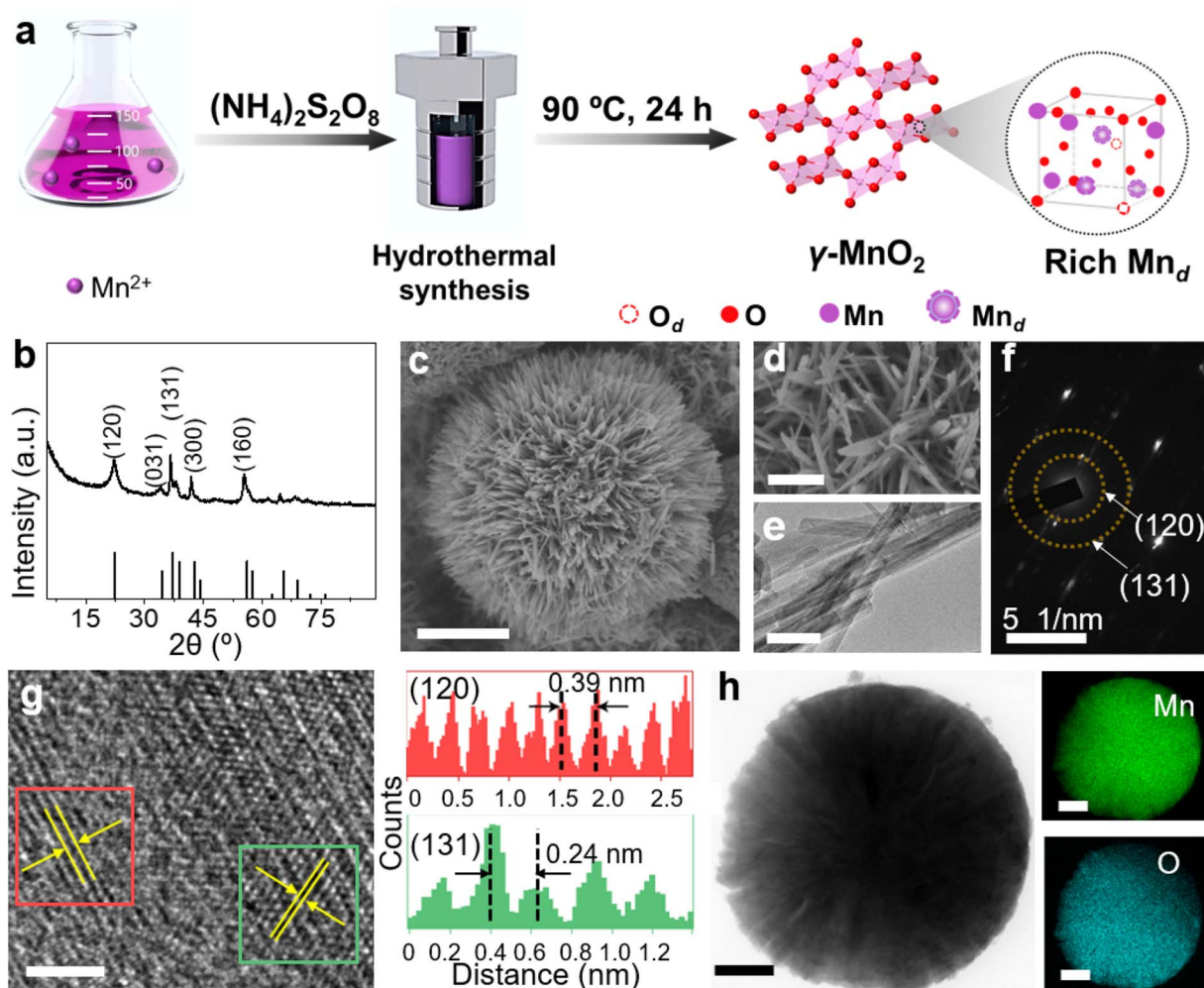


**Fig. 1** (a) Schematic synthesis process of  $\gamma$ - $\text{MnO}_2$  catalysts with Mn defects ( $\text{Mn}_d$ ). (b) PXRD pattern, (c and d) SEM images, (e) TEM image, (f) SAED pattern, and (g) HRTEM image (left) and corresponding intensity plot (right) of  $\gamma$ - $\text{MnO}_2$  catalyst. (h) EDX elemental maps showing the distributions of Mn and O. Scale bars: (c) 2  $\mu\text{m}$ , (d) 500 nm, (e) 50 nm, (g) 2 nm, (h) 1  $\mu\text{m}$ .

the hydrothermal process, while the  $\text{Mn}^{3+}$  species remain almost constant (Fig. S10†). The nearly unchanged ratio of  $\text{Mn}^{3+}/\text{Mn}^{4+}$ , despite the differing amounts of  $\text{O}_d$  species in  $\alpha$ - $\text{MnO}_2(1)$  and  $\alpha$ - $\text{MnO}_2(10)$ , may be attributed to the presence of N anionic residues. The detailed mechanisms of  $\text{O}_d$  species formation are beyond the scope of the current stage of study and will be pursued in our future work.

To demonstrate the practicality of our approach, we conducted a gram-scale oxidation of vanillyl alcohol to vanillin in an aqueous environment as a model reaction, and the results are presented in Table 1. For the catalytic reaction, 0.77 g of vanillyl alcohol, 6.0 mL of  $\text{H}_2\text{O}$ , and 10.0 mmol of catalyst were added to a quartz reactor and stirred at room temperature under sunlight for 10 h while exposed to air. No product is obtained in the absence of a catalyst (Table 1, entry 1). The as-prepared  $\text{MnO}_2$  catalysts, including  $\alpha$ -,  $\beta$ -,  $\varepsilon$ -, and  $\gamma$ - $\text{MnO}_2$  (Table 1, entries 2–9), are found to be active for the oxidation of vanillyl alcohol to vanillin.  $\text{MnO}_2$  catalysts with more abundant  $\text{O}_d$  (Fig. 2d), such as  $\alpha$ - $\text{MnO}_2(1)$  and  $\alpha$ - $\text{MnO}_2(10)$ , exhibit lower catalytic performance compared to  $\alpha$ - $\text{MnO}_2$  with fewer  $\text{O}_d$ ,

indicating that  $\text{O}_d$  species are not a key factor in promoting the catalytic activity of  $\text{MnO}_2$  catalysts for the oxidation under sunlight. The  $\gamma$ - $\text{MnO}_2$  catalyst exhibits the highest catalytic activity and vanillin selectivity, converting vanillyl alcohol to vanillin with a yield of nearly 90% (Table 1, entry 2), outperforming the  $\gamma$ - $\text{MnO}_2(1)$  and  $\gamma$ - $\text{MnO}_2(10)$  catalysts (Table 1, entries 3,4). Since  $\gamma$ - $\text{MnO}_2$ ,  $\gamma$ - $\text{MnO}_2(1)$ , and  $\gamma$ - $\text{MnO}_2(10)$  catalysts have similar surface  $\text{O}_d$  species (Fig. 2c), Brunauer–Emmett–Teller (BET) surface areas (Fig. S6†), and surface morphologies (Fig. 1c, d and S4†), the superior catalytic performance of the  $\gamma$ - $\text{MnO}_2$  catalyst among them can be attributed to the most abundant  $\text{Mn}_d$  species on the surface (Fig. 3a). Similarly, the best vanillin selectivity and superior catalytic performance displayed by  $\gamma$ - $\text{MnO}_2$ , compared to other  $\text{MnO}_2$  catalysts with diverse crystal structures (Table 1, entries 2–5 and 9–10), can be attributed to the prevalence of its  $\text{Mn}_d$  species (Fig. 3). Given the significant influence of factors, such as solvent and temperature, on the catalytic oxidation reaction of vanillyl alcohol,<sup>38</sup> we explored various conditions using the  $\gamma$ - $\text{MnO}_2$  catalyst to determine the optimal reaction parameters.





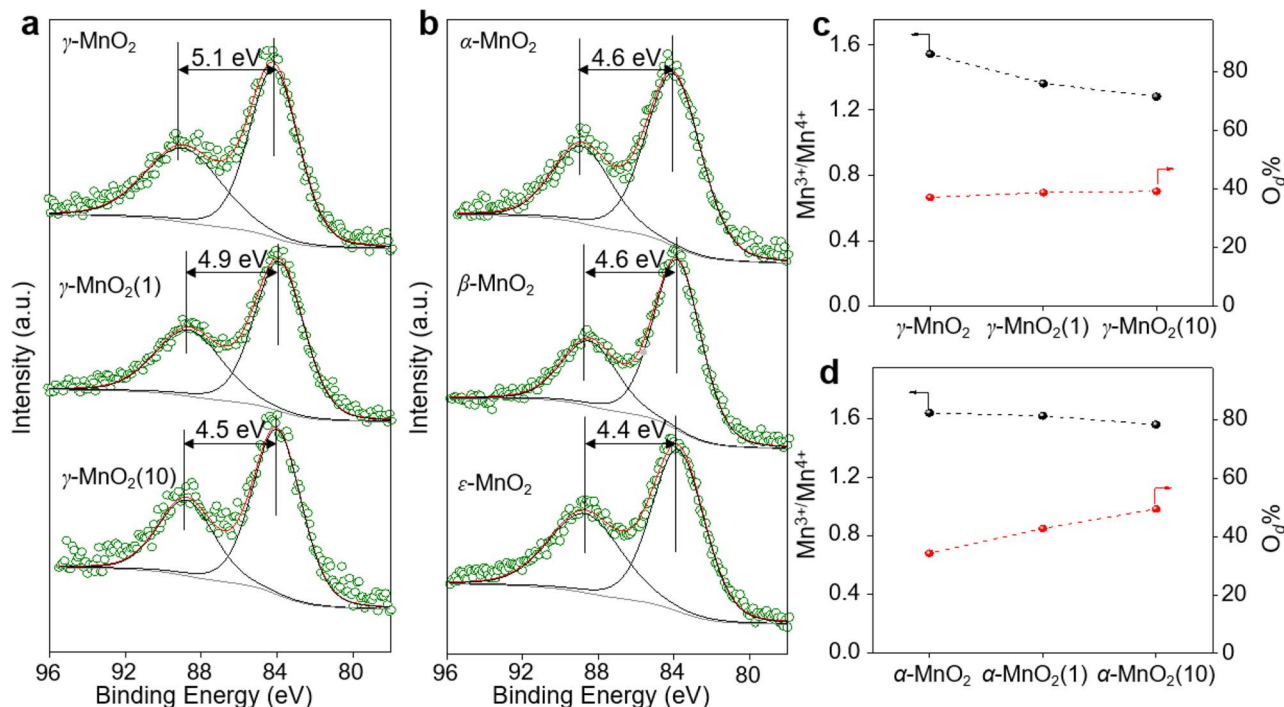


Fig. 2 Mn 3s XPS spectra for (a)  $\gamma$ -MnO<sub>2</sub> with different amounts of urea added in the synthesis and (b) MnO<sub>2</sub> with different crystal structures. The molar ratio of Mn<sup>3+</sup>/Mn<sup>4+</sup> and percentage of oxygen defects (O<sub>d</sub>) in different (c)  $\gamma$ -MnO<sub>2</sub> and (d)  $\alpha$ -MnO<sub>2</sub>.

Table 1 Oxidation of vanillyl alcohol to vanillin over various catalysts

Entry	Catalyst	Con.%	Sel.% <sup>a</sup>	Yield%
1	—	n.d.	—	—
2	$\gamma$ -MnO <sub>2</sub>	93.4	95.7	89.4
3	$\gamma$ -MnO <sub>2</sub> (1)	66.3	95.5	63.3
4	$\gamma$ -MnO <sub>2</sub> (10)	63.3	94.9	60.1
5	$\alpha$ -MnO <sub>2</sub>	60.8	86.3	52.5
6	$\alpha$ -MnO <sub>2</sub> (1)	25.5	45.7	11.7
7	$\alpha$ -MnO <sub>2</sub> (10)	26.0	54.0	14.0
8	$\beta$ -MnO <sub>2</sub>	63.0	94.4	59.5
9	$\epsilon$ -MnO <sub>2</sub>	61.4	91.3	56.1

<sup>a</sup> Selective generation of vanillin. Reaction conditions: vanillyl alcohol (0.77 g), Solvent (H<sub>2</sub>O, 6.0 mL), catalyst 10.0 mmol, open to air, sunlight, 30 °C, 10 h. (n.d. = Not detected).

The  $\gamma$ -MnO<sub>2</sub> catalyst exhibits remarkably superior catalytic performance at 30 °C (Table S2†) and when using H<sub>2</sub>O as a solvent (Table S3†). The significant improvement in the catalytic performance of  $\gamma$ -MnO<sub>2</sub> catalyst in H<sub>2</sub>O compared to other solvents (Table S3†) may be attributed to the role of H<sub>2</sub>O in activating O<sub>2</sub>/H<sub>2</sub>O to form key active O species, as discussed in the following section on the mechanism.

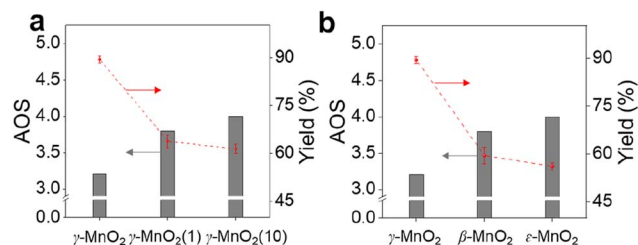


Fig. 3 Catalytic performance of  $\gamma$ -MnO<sub>2</sub> and comparison catalysts for oxidation of vanillyl alcohol to vanillin. (a) AOS-yield of vanillin on  $\gamma$ -MnO<sub>2</sub>, (b) AOS-yield of vanillin on MnO<sub>2</sub> with various crystal structures.

To elucidate its superior catalytic performance, the catalytic mechanism of the oxidation of vanillyl alcohol over the  $\gamma$ -MnO<sub>2</sub> catalyst was evaluated. In comparison to the impressive catalytic performance under O<sub>2</sub> (Fig. 4a, eqn (1)), the oxidation of vanillyl alcohol is dramatically suppressed (~6.5% yield of vanillin) when the reaction is performed under N<sub>2</sub> (Fig. 4a, eqn (2)), confirming that oxidation over the  $\gamma$ -MnO<sub>2</sub> catalyst mainly occurs through a dissolved oxygen species-mediated route.<sup>39</sup> After the reaction under the N<sub>2</sub> atmosphere, the ratio of surface Mn<sup>3+</sup>/Mn<sup>4+</sup> species increases from 1.54 to 1.63 (Fig. S11†), indicating the involvement of Mn species in the catalytic cycle.

Considering the importance of oxygen in determining oxidative activity, we further elucidate the role of dissolved oxygen species in sunlight oxidation through scavenger control experiments. Despite the addition of furfuryl alcohol (FFA, an efficient scavenger of <sup>1</sup>O<sub>2</sub>) to the reactants, the yield of vanillin is 89.4% (Fig. 4a, eqn (3)), indicating that FFA does not affect

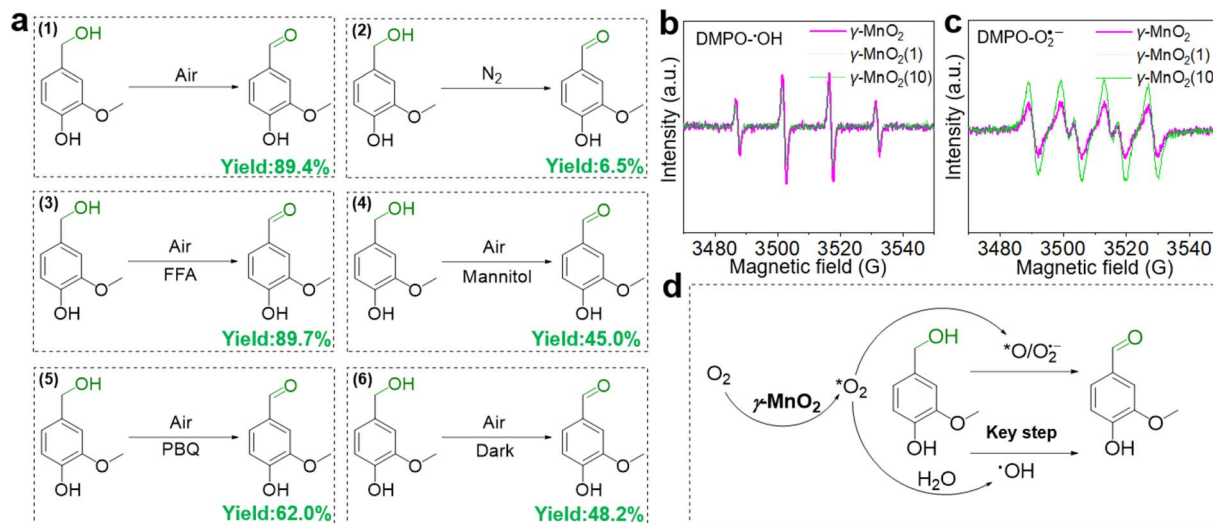


Fig. 4 Exploring the role of oxygen species in the oxidation of vanillyl alcohol over  $\gamma$ -MnO<sub>2</sub> catalyst. (a) Oxidation of vanillyl alcohol under different atmospheres or with various quenchers. (b and c) EPR spectra of DMPO-·OH and DMPO-O<sub>2</sub>·<sup>-</sup> over various  $\gamma$ -MnO<sub>2</sub> catalysts. (d) Proposed the role of oxygen species in the oxidation of vanillyl alcohol. \*O<sub>2</sub> refers to the adsorbed oxygen.

the activity of the  $\gamma$ -MnO<sub>2</sub> catalyst. On the other hand, mannitol (an efficient scavenger of ·OH) causes a significant decrease in the yield of vanillin (~45.0%) (Fig. 4a, eqn (4)). With 1,4-Benzoquinone (PBQ, an efficient scavenger of O<sub>2</sub>·<sup>-</sup>) added during the reaction, only a normal conversion inhibition of vanillyl alcohol is observed and ~62.0% yield of vanillin is obtained (Fig. 4a, eqn (5)). The above analyses confirm that the oxidation of vanillyl alcohol to vanillin under sunlight occurs with the assistance of O<sub>2</sub>·<sup>-</sup> and ·OH species derived from O<sub>2</sub>/H<sub>2</sub>O activation by the  $\gamma$ -MnO<sub>2</sub> catalyst.

Electron paramagnetic resonance (EPR) was employed to confirm the presence of O<sub>2</sub>·<sup>-</sup> and ·OH species during the oxidation process.<sup>40</sup> Under the reaction conditions, a quadruple peak with an intensity ratio of 1:2:2:1 is observed for the characteristic peak of pyrroline nitrogen oxide (DMPO)·OH (Fig. 4b).<sup>41</sup> Another quadruple peak with an intensity ratio of 1:1:1:1 is observed for the characteristic peak of DMPO-O<sub>2</sub>·<sup>-</sup> (Fig. 4c),<sup>42</sup> indicating the formation of O<sub>2</sub>·<sup>-</sup> and ·OH species. Notably, the peak intensity of DMPO·OH over the  $\gamma$ -MnO<sub>2</sub> catalyst with superior catalytic activity is stronger than that of  $\gamma$ -MnO<sub>2</sub>(1) and  $\gamma$ -MnO<sub>2</sub>(10) catalysts with mediocre activity. In contrast, the intensities of DMPO-O<sub>2</sub>·<sup>-</sup> over the  $\gamma$ -MnO<sub>2</sub> catalyst shows opposite trends. These results further support that ·OH species are the key reactive oxygen species in the oxidation reaction of vanillyl alcohol *via*  $\gamma$ -MnO<sub>2</sub> under sunlight (Fig. 4d), consistent with the results in Fig. 4a. Meanwhile, the stronger DMPO·OH signal for  $\gamma$ -MnO<sub>2</sub> compared to the other two samples indicates enhanced ·OH generation due to the rich-Mn<sub>d</sub>. Interestingly, under dark conditions, the  $\gamma$ -MnO<sub>2</sub> catalyst achieves a ~48.2% yield of vanillin (Fig. 4a, eqn (6)), similar to the 45.0% yield obtained when mannitol is added to the reaction mixture (Fig. 4a, eqn (4)). Additionally, the  $\gamma$ -MnO<sub>2</sub> catalyst exhibits broad light absorption from ultraviolet to visible light, effectively covering most of the solar spectrum (Fig. S12†). This

characteristic enables the abundant generation of ·OH species under natural light exposure at 30 °C.

Based on the above analysis, O<sub>2</sub>, H<sub>2</sub>O, and sunlight emerge as key factors influencing the catalytic performance of the  $\gamma$ -MnO<sub>2</sub> catalyst in the oxidation of vanillyl alcohol to vanillin. Previous studies have demonstrated that ·OH species can be generated from H<sub>2</sub>O/O<sub>2</sub> mixtures on  $\delta$ -MnO<sub>2</sub> or Mn/Na<sub>2</sub>WO<sub>4</sub>/SiO<sub>2</sub> catalysts under sunlight conditions.<sup>43,44</sup> To verify the formation of ·OH species in H<sub>2</sub>O/O<sub>2</sub> mixtures over the  $\gamma$ -MnO<sub>2</sub> catalyst, *in situ* IR spectroscopy was employed, and the results are depicted in Fig. 5. The stretching vibration peaks of ·OH species at ~2820, 3711, 3735 and 3750 cm<sup>-1</sup> intensify with prolonged sunlight illumination (Fig. 5). However, the stretching vibration of ·OH species is not observed in the absence of H<sub>2</sub>O (Fig. 5a, black curve) or under dark conditions (Fig. 5a, blue curve). These results indicate that both H<sub>2</sub>O and sunlight play crucial roles in the formation of ·OH species in H<sub>2</sub>O/O<sub>2</sub> mixtures. In the oxidation reaction, oxygen is considered to be the ideal oxidant, with H<sub>2</sub>O and H<sub>2</sub>O<sub>2</sub> identified as by-products. Identifying these by-products is vital for elucidating the reaction

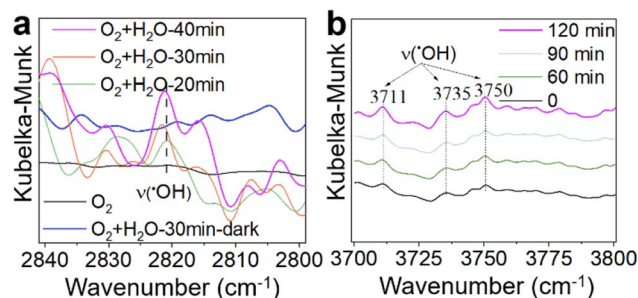


Fig. 5 *In situ* diffuse reflectance IR spectra (DRIFTS) of activation of O<sub>2</sub>/H<sub>2</sub>O over  $\gamma$ -MnO<sub>2</sub> catalyst. (a) Activation of O<sub>2</sub>/H<sub>2</sub>O under various conditions. (b) Activation of O<sub>2</sub>/H<sub>2</sub>O under sunlight illumination.

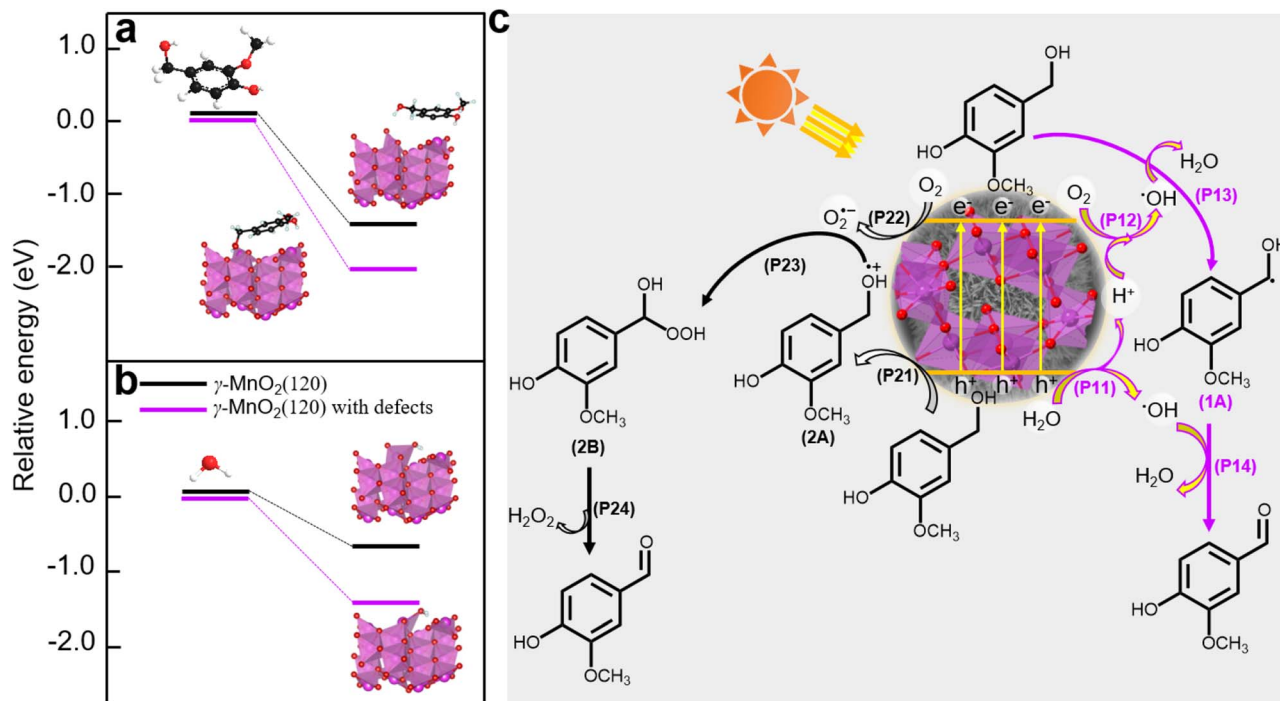


Fig. 6 (a) DFT calculations for vanillyl alcohol adsorbed on  $\gamma$ -MnO<sub>2</sub> catalyst with/without defects. (b) DFT calculations for H<sub>2</sub>O adsorbed on  $\gamma$ -MnO<sub>2</sub> catalyst with/without defects. (c) A plausible mechanism of oxidation of vanillyl alcohol to vanillin over  $\gamma$ -MnO<sub>2</sub> catalyst under air atmosphere.

mechanism, especially as  $\cdot\text{OH}$  species could be produced from H<sub>2</sub>O<sub>2</sub> species. Further investigation into the by-product of H<sub>2</sub>O<sub>2</sub> species was conducted using the iodometry method, and the results are presented in Fig. S13.† A peak at  $\sim 365$  nm, assigned to the formation of H<sub>2</sub>O<sub>2</sub>, is detected under sunlight illustration. However, H<sub>2</sub>O<sub>2</sub> species are not produced under dark conditions. Similar results are obtained in the absence of a reactant or  $\gamma$ -MnO<sub>2</sub> catalyst. These findings confirm that H<sub>2</sub>O<sub>2</sub> species, as a by-product, are produced during the oxidation of vanillyl alcohol to vanillin over the  $\gamma$ -MnO<sub>2</sub> catalyst with the assistance of sunlight illustration.

Density functional theory (DFT) calculations were employed to elucidate the absorption sites on the  $\gamma$ -MnO<sub>2</sub> catalyst, comprising a perfect (120) facet and defective (120) facets (Fig. S14†). The DFT calculations (Fig. 6a and b) reveal that vanillyl alcohol and H<sub>2</sub>O preferentially adsorb on the Mn<sub>d</sub> species (Mn<sup>3+</sup> species) of defective (120) facets, regardless of the presence of O<sub>d</sub> species for both models. The preference of vanillyl alcohol for adsorption on the Mn<sub>d</sub> species is further supported by DFT calculations in Fig. 6a and S15,† illustrating the interaction between Mn<sup>3+</sup> species of MnO<sub>2</sub> and vanillyl alcohol. This interaction results in an adsorption energy of  $-217.3$  kJ mol<sup>-1</sup> (Fig. S15†), significantly exceeding the adsorption energy of  $-131.5$  kJ mol<sup>-1</sup> observed for MnO<sub>2</sub> featuring only O<sub>d</sub> sites. Similarly, H<sub>2</sub>O exhibits a preference for adsorption on the Mn<sub>d</sub> species rather than O<sub>d</sub> sites, as depicted in Fig. 6b. Furthermore, oxygen molecules from the air can also be absorbed by the Mn<sub>d</sub>. Previous studies have reported the adsorption of oxygen molecules on Mn<sub>d</sub> in MnO<sub>2</sub> catalysts.<sup>45</sup>

Based on the analysis and insights gleaned from previous studies,<sup>10,46,47</sup> we propose a plausible mechanism for the oxidation of vanillyl alcohol to vanillin using the  $\gamma$ -MnO<sub>2</sub> catalyst in air (Fig. 6c). In this mechanism, O<sub>2</sub>, H<sub>2</sub>O, and vanillyl alcohol are simultaneously adsorbed onto the catalyst. Under sunlight illumination, electrons (e<sup>-</sup>) and holes (h<sup>+</sup>) are separated from the surface of the  $\gamma$ -MnO<sub>2</sub> catalyst. During this step, adsorbed H<sub>2</sub>O accepts holes (h<sup>+</sup>) to form  $\cdot\text{OH}$  species, releasing H<sup>+</sup> species (P11, Fig. 6c). Simultaneously, vanillyl alcohol accepts holes (h<sup>+</sup>) to generate alcohol radical species (2A) (P21, Fig. 6c). Adsorbed oxygen can accept e<sup>-</sup> from the  $\gamma$ -MnO<sub>2</sub> catalyst surface to form O<sub>2</sub><sup>-•</sup> species (P22, Fig. 6c), or it can combine with protons generated from P11 to form  $\cdot\text{OH}$  species (P12, Fig. 6c). The formation of  $\cdot\text{OH}$  species from O<sub>2</sub> and H<sub>2</sub>O in oxide-based catalysts, including MnO<sub>2</sub>, has also been proposed.<sup>44,48</sup> Vanillyl alcohol radical (1A, Fig. 6c) is selectively obtained by combining the adsorbed vanillyl alcohol with  $\cdot\text{OH}$  species (P13, Fig. 6c), which further converts to vanillin through a subsequent reaction with  $\cdot\text{OH}$  species (P14, Fig. 6c). The positive radical of vanillyl alcohol (2A, Fig. 6c) reacts with O<sub>2</sub><sup>-•</sup> species to produce the alcohol peroxo species (2B) (P23, Fig. 6c), eventually converting to vanillin and releasing H<sub>2</sub>O<sub>2</sub> (P24, Fig. 6c). Under these conditions, the catalytic cycle is completed, and the  $\gamma$ -MnO<sub>2</sub> catalyst is ready for the next catalytic process.

## Conclusions

In summary, we have successfully fabricated manganese oxide-based catalysts with different Mn defects on MnO<sub>2</sub> with various



crystal structures and on  $\gamma$ -MnO<sub>2</sub> with different amounts of urea. Comprehensive structural characterization highlights the significance of urea in tuning the coordination environment of Mn species in  $\gamma$ -MnO<sub>2</sub> and the O species in  $\alpha$ -MnO<sub>2</sub>. In the gram-scale oxidation of vanillyl alcohol to vanillin, the Mn-defected  $\gamma$ -MnO<sub>2</sub> catalyst demonstrates excellent photocatalytic performance compared to the O-defected  $\alpha$ -MnO<sub>2</sub> catalyst and other type ( $\beta$ ,  $\epsilon$ )-MnO<sub>2</sub> catalysts. DFT calculations and control experiments demonstrate that the defected-Mn species in the  $\gamma$ -MnO<sub>2</sub> catalyst facilitate the adsorption of vanillyl alcohol and H<sub>2</sub>O, which converts to the corresponding 'OH species under natural light illumination. The synergistic effect of the Mn-defected species and 'OH species plays a crucial role in enhancing the photocatalytic performance in the aerobic oxidation of vanillyl alcohol to vanillin over the  $\gamma$ -MnO<sub>2</sub> catalyst. This study not only presents effective methods for tuning the coordination environments of Mn atoms in MnO<sub>2</sub> for the selective oxidation of vanillyl alcohol to vanillin but also provides valuable insights for the development of advanced transition metal oxide photocatalysts.

## Author contributions

Q. Ke, Y. Zhang and C. Wan: conceptualization, methodology, and writing – original draft. Y. Zhang, J. Tang, S. Li, X. Guo, T. Hamada, and S. M. Osman: data curation, chemical experiments, and formal analysis. Q. Ke, and C. Wan: funding acquisition and investigation. C. Wan, M. Han, Y. Kang, and Y. Yamauchi: supervision and writing – review & editing.

## Conflicts of interest

There are no conflicts to declare.

## Acknowledgements

Dr Y. K. thanks the support from JSPS Postdoctoral Fellowships for Research in Japan. This work was financially supported by the National Natural Science Foundation of China (22108238, 22302001), Key Projects of the Department of Education of Anhui Province of China (RZ2000003450, 2022AH050314), the Anhui Provincial Natural Science Foundation of China (2008085MB47), the China Postdoctoral Science Foundation (2019M662060, 2020T130580, PC2022046), the Scientific Research Training Program for College Students of Anhui University of Technology (202110360040, S202110360213), the JST-ERATO Yamauchi Materials Space-Tectonics Project (JPMJER2003), the Researchers Supporting Project RSP2023R405 (King Saud University, Saudi Arabia), and the UQ-Yonsei International Research Project (*via* UQ). The authors also thank Shiyanjia Lab (<https://www.shiyanjia.com/>) for the support of the XRD, XPS, and BET tests. This work used the Queensland node of the NCRIS-enabled Australian National Fabrication Facility (ANFF). We express our gratitude for English editing software, such as Grammarly and ChatGPT, for refining language and checking grammatical errors in our manuscript.

## References

- 1 R. Singathi, R. Raghunathan, R. Krishnan, S. K. Rajendran, S. Baburaj, M. P. Sibi, D. C. Webster and J. Sivaguru, *Angew. Chem., Int. Ed.*, 2022, **61**, e202203353.
- 2 B. Schaefer, *Natural Products in the Chemical Industry*, Springer, Berlin, 2014.
- 3 X. Shen, Q. Meng, Q. Mei, H. Liu, J. Yan, J. Song, D. Tan, B. Chen, Z. Zhang, G. Yang and B. Han, *Chem. Sci.*, 2020, **11**, 1347–1352.
- 4 Z. Xiang, W. Han, J. Deng, W. Zhu, Y. Zhang and H. Wang, *ChemSusChem*, 2020, **13**, 4199–4213.
- 5 D. Zhu, L. Xu, S. Sethupathy, H. Si, F. Ahmad, R. Zhang, W. Zhang, B. Yang and J. Sun, *Green Chem.*, 2021, **23**, 9554–9570.
- 6 W. Sun, S. Wu, Y. Lu, Y. Wang, Q. Cao and W. Fang, *ACS Catal.*, 2020, **10**, 7699–7709.
- 7 Z. Pan, A. Puente-Urbina, A. Bodi, J. A. van Bokhoven and P. Hemberger, *Chem. Sci.*, 2021, **12**, 3161–3169.
- 8 M. Fache, B. Boutevin and S. Caillol, *ACS Sustainable Chem. Eng.*, 2016, **4**, 35–46.
- 9 M. B. Figueirêdo, I. Hita, P. J. Deuss, R. H. Venderbosch and H. J. Heeres, *Green Chem.*, 2022, **24**, 4680–4702.
- 10 B.-C. Li, N. N. Huy, J.-Y. Lin, S. Phattarapattamawong, G. Lisak, H. Wang and K.-Y. A. Lin, *J. Environ. Chem. Eng.*, 2021, **9**, 106092.
- 11 R. Zhang, R. Maltari, M. Guo, J. Kontro, A. Eronen and T. Repo, *Ind. Crops Prod.*, 2020, **145**, 112095.
- 12 J. Dai, A. F. Patti, G. N. Styles, S. Nanayakkara, L. Spiccia, F. Arena, C. Italiano and K. Saito, *Green Chem.*, 2019, **21**, 2005–2014.
- 13 B. N. Zope, D. D. Hibbitts, M. Neurock and R. J. Davis, *Science*, 2010, **330**, 74–78.
- 14 C.-R. Chang, X.-F. Yang, B. Long and J. Li, *ACS Catal.*, 2013, **3**, 1693–1699.
- 15 X. Cao, A. Huang, C. Liang, H.-C. Chen, T. Han, R. Lin, Q. Peng, Z. Zhuang, R. Shen, H. M. Chen, Y. Yu, C. Chen and Y. Li, *J. Am. Chem. Soc.*, 2022, **144**, 3386–3397.
- 16 J. Li, H. Yuan, Q. Zhang, K. Luo, Y. Liu, W. Hu, M. Xu and S. Xu, *Phys. Chem. Chem. Phys.*, 2020, **22**, 27272–27279.
- 17 D. A. Kitchaev, S. T. Dacek, W. Sun and G. Ceder, *J. Am. Chem. Soc.*, 2017, **139**, 2672–2681.
- 18 X. Zeng, G. Cheng, Q. Liu, W. Yu, R. Yang, H. Wu, Y. Li, M. Sun, C. Zhang and L. Yu, *Ind. Eng. Chem. Res.*, 2019, **58**, 13926–13934.
- 19 J. C. Hunter, *J. Solid State Chem.*, 1981, **39**, 142–147.
- 20 X. Luo, X. Tang, J. Ni, B. Wu, C. Li, M. Shao and Z. Wei, *Chem. Sci.*, 2023, **14**, 1679–1686.
- 21 X. Yan, T. Gan, S. Shi, J. Du, G. Xu, W. Zhang, W. Yan, Y. Zou and G. Liu, *Catal. Sci. Technol.*, 2021, **11**, 6369–6373.
- 22 K.-Y. A. Lin, W.-D. Oh, M.-W. Zheng, E. Kwon, J. Lee, J.-Y. Lin, X. Duan and F. Ghanbari, *J. Colloid Interface Sci.*, 2021, **592**, 416–429.
- 23 S. Ndayiragije, Y. Zhang, Y. Zhou, Z. Song, N. Wang, T. Majima and L. Zhu, *Appl. Catal., B*, 2022, **307**, 121168.



- 24 C. Wang, Y. Zeng, X. Xiao, S. Wu, G. Zhong, K. Xu, Z. Wei, W. Su and X. Lu, *J. Energy Chem.*, 2020, **43**, 182–187.
- 25 L. Ni, Z. Wu, G. Zhao, C. Sun, C. Zhou, X. Gong and G. Diao, *Small*, 2017, **13**, 1603466.
- 26 F. Lai, J. Feng, R. Yan, G. C. Wang, M. Antonietti and M. Oschatz, *Adv. Funct. Mater.*, 2018, **28**, 1801298.
- 27 Y. Li, X. Wei, S. Han, L. Chen and J. Shi, *Angew. Chem., Int. Ed.*, 2021, **60**, 21464–21472.
- 28 A. Singh, O. Sel, H. Perrot, V. Balland, B. Limoges and C. Laberty-Robert, *J. Mater. Chem. A*, 2021, **9**, 1500–1506.
- 29 Z. Zhou, X. Zheng, M. Liu, P. Liu, S. Han, Y. Chen, B. Lan, M. Sun and L. Yu, *ChemSusChem*, 2022, **15**, e202200612.
- 30 Q. Zhang, G. Xie, M. Duan, Y. Liu, Y. Cai, M. Xu, K. Zhao, H. Tai, Y. Jiang and Y. Su, *ACS Appl. Nano Mater.*, 2023, **6**, 17445–17456.
- 31 J. Tang, J. Chen, Z. Zhang, Q. Ma, X. Hu, P. Li, Z. Liu, P. Cui, C. Wan, Q. Ke, L. Fu, J. Kim, T. Hamada, Y. Kang and Y. Yamauchi, *Chem. Sci.*, 2023, **14**, 13402–13409.
- 32 H. Liu, W. Jia, X. Yu, X. Tang, X. Zeng, Y. Sun, T. Lei, H. Fang, T. Li and L. Lin, *ACS Catal.*, 2021, **11**, 7828–7844.
- 33 Q. Ke, Y. Jin, F. Ruan, M. N. Ha, D. Li, P. Cui, Y. Cao, H. Wang, T. Wang, V. N. Nguyen, X. Han, X. Wang and P. Cui, *Green Chem.*, 2019, **21**, 4313–4318.
- 34 D. Sun, L. Peng, Y. Yang, Y. Fang, S. P. Jiang and Z. Shao, *J. Catal.*, 2022, **409**, 48–58.
- 35 C. Chen, G. Xie, J. Dai, W. Li, Y. Cai, J. Li, Q. Zhang, H. Tai, Y. Jiang and Y. Su, *Nano Energy*, 2023, **116**, 108788.
- 36 A. V. Emeline, N. V. Sheremetyeva, N. V. Khomchenko, V. K. Ryabchuk and N. Serpone, *J. Phys. Chem. C*, 2007, **111**, 11456–11462.
- 37 Y. Liu, M.-S. Niu, X. Yi, G. Li, H. Zhou and W. Gao, *Appl. Surf. Sci.*, 2021, **561**, 150081.
- 38 J. Estrada-Pomares, S. Ramos-Terrón, G. Lasarte-Aragónés, R. Lucena, S. Cárdenas, D. Rodríguez-Padrón, R. Luque and G. de Miguel, *J. Mater. Chem. A*, 2022, **10**, 11298–11305.
- 39 F. Li, J. Tang, Q. Ke, Y. Guo, M. N. Ha, C. Wan, Z. Lei, J. Gu, Q. Ling, V. N. Nguyen and W. Zhan, *ACS Catal.*, 2021, **11**, 11855–11866.
- 40 J. Li, G. Xie, J. Jiang, Y. Liu, C. Chen, W. Li, J. Huang, X. Luo, M. Xu, Q. Zhang, M. Yang and Y. Su, *Nano Energy*, 2023, **108**, 108234.
- 41 S. Mu, H. Lu, Q. Wu, L. Li, R. Zhao, C. Long and C. Cui, *Nat. Commun.*, 2022, **13**, 3694.
- 42 Y. Yang, B. Cheng, J. Yu, L. Wang and W. Ho, *Nano Res.*, 2023, **16**, 4506–4514.
- 43 S. Das, A. Samanta and S. Jana, *ACS Sustainable Chem. Eng.*, 2017, **5**, 9086–9094.
- 44 K. Takanabe and E. Iglesia, *Angew. Chem., Int. Ed.*, 2008, **47**, 7689–7693.
- 45 J. Shi, T. Qi, B.-C. Sun, G.-W. Chu and J.-F. Chen, *Chem. Eng. J.*, 2022, **440**, 135802.
- 46 Q. Zhu, P. Zhan, C. Zhang, R. Chen, C. Ren, H. Zhao, W. Ren, J. Zhang, P. Qin and D. Cai, *ChemPhotoChem*, 2023, **7**, e202200337.
- 47 M. Bellardita, S. Yurdakal, B. S. Tek, Ç. Değirmenci, G. Palmisano, V. Loddo, L. Palmisano, J. Soria, J. Sanz and V. Augugliaro, *J. Environ. Chem. Eng.*, 2021, **9**, 105308.
- 48 S. Zhao, Y. Wen, X. Liu, X. Pen, F. Lü, F. Gao, X. Xie, C. Du, H. Yi D. Kang and X. Tang, *Nano Res.*, 2020, **13**, 1544–1551.

